Catalytic Pyroprotein Seed Layers for Sodium Metal Anodes

Min Eui Lee,[†,§] Hyo Won Kwak,[†,⊥,§] Jin Hwan Kwak,[‡] Hyoung-Joon Jin,*[,†] and Young Soo Yun*[,‡]

†Department of Polymer Science and Engineering, Inha University, Incheon 22212, South Korea
‡Department of Chemical Engineering, Kangwon National University, Samcheok 25913, South Korea

Ⓢ Supporting Information

ABSTRACT: We report a pyroprotein seed layer (PSL, ~100 nm in thickness)-coated Cu foil electrode (PSL-Cu) demonstrating highly reversible Na metal storage behavior with a mean Coulombic efficiency (CE) of ~99.96% over 300 cycles in a glyme-based electrolyte. Via a synergistic effect with the electrolyte, the carbonaceous thin film containing numerous nucleophilic active sites guides the homogeneous Na metal deposition/stripping process with the formation of numerous catalytic seeds, resulting in remarkably stable cycling and a low Na metal nucleation overpotential of ~10 mV. In addition, the CE deviation values of the PSL-Cu electrode were ~0.43% in several cell tests, demonstrating its reliable cycling behavior with low cell-to-cell variation. The

practicality of PSL-Cu was further demonstrated via full-cell experiments with a polyanion cathode, in which it achieved a high specific power density and energy density of 3,800 W kg^{-1} and ~402 W h kg^{-1}, respectively. This work provides a simple process for the fabrication of a Na metal anode.

KEYWORDS: pyroprotein, carbon thin film, catalytic seed layer, metal anode, sodium-ion batteries
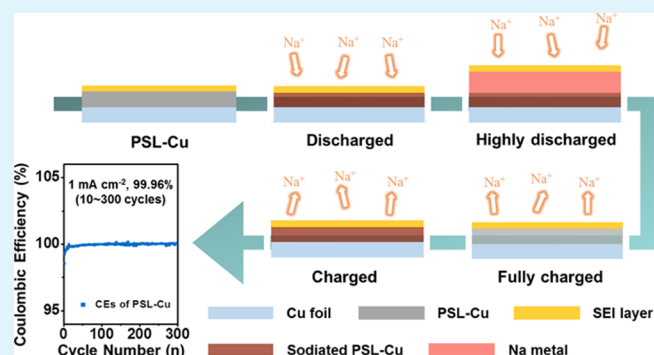
INTRODUCTION

Sodium-ion batteries (NIBs) have drawn a lot of attention as a promising post-Li-ion batteries (LIBs) owing to their well-known redox properties, which are similar to those of LIBs, and the ubiquity of Na resources.[1,2] For the practical application of NIBs, one of the major obstacles is the absence of realizable anode materials exhibiting high reversible capacities, low redox potentials, high Coulombic efficiencies (CEs), high rate capabilities, and stable cycling performances.[1−3] Extensive research efforts are being devoted to developing a new active material with high performance, and various anode materials have been reported.[4−20] Hard carbons,[4,5] nanostructured sp^2 carbon materials,[6−9] conversion and/or alloying materials based on metal oxide/sulfide/phosphide,[10−16] alloying materials,[17−19] and others[20−24] have been reported in the past several years. However, the reported materials do not exhibit the requisite CE, volumetric/gravimetric energy efficiency, and/or cycle life. To maintain stable cycling over several hundreds of cycles, CEs of more than 99.9 are required. Additionally, in order for NIBs to be used as an alternative power source to LIBs, anode materials with volumetric/gravimetric energy efficiencies that surpass those of graphite in LIBs are needed. In addition, except for carbon-based materials, the synthetic processes and material costs of the reported anode materials render them uncompetitive for potential large-scale application of NIBs in fields such as uninterruptible power supply systems, electric

vehicles, and grid systems. Sodium metal can deliver a significantly high capacity of 1166 mA h g^{-1} at a redox potential of −2.71 V versus SHE but suffers from a low CE and safety issues caused by dendritic metal growth.[25−29] During the charging process, high aspect ratio dendritic metals are grown with the formation of a large amount of solid electrolyte interface (SEI) layers, one side of which is connected to the conducting substrate. The contact area of the dendritic metals is preferentially removed during the discharge process, causing mossy dead Na metal byproducts.[29] Owing to the mossy dead Na metal byproducts, which are nonconducting and inactive, the CE decreases and the cell resistance increases. In addition, the repetitive formation/deformation cycles of the high-surface-area dendritic metals induce continuous electrolyte decomposition, causing the exhaustion of the electrolyte and a reduction in the CE.[25] Notably, Cui's group reported that a glyme-based electrolyte is slightly decomposed in a metal deposition/stripping process and can obstruct dendritic Na metal overgrowth.[26] Through the formation of a homogeneous, inorganic SEI layer composed of sodium oxide and sodium fluoride, which was highly impervious to the glyme solvent, they achieved average CEs of about 99.9% and stability during 300 cycles at an areal current density of 0.5 mA cm^{-2}.[26]
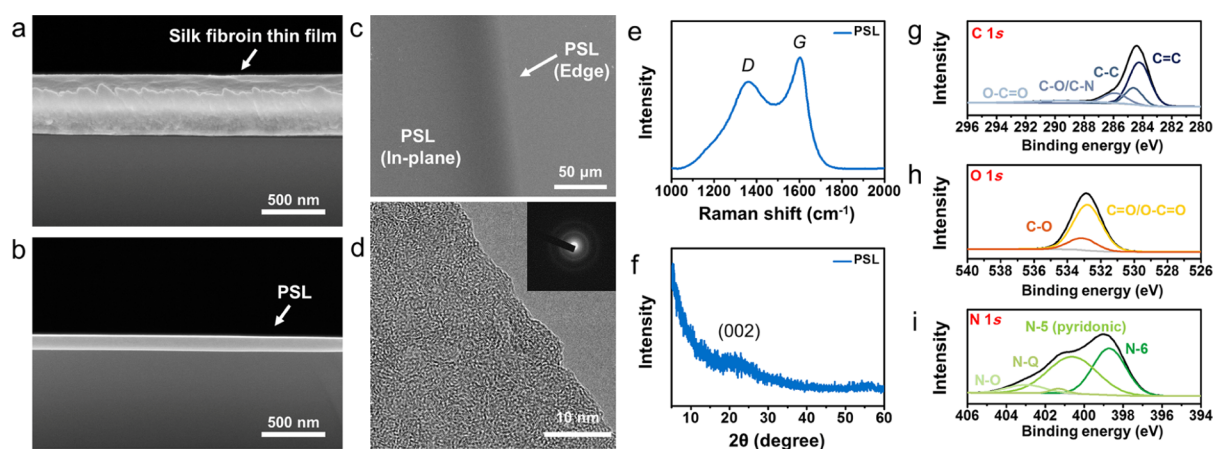
Figure 1. FE-SEM images of (a) silk fibroin thin film, (b) PSL fracture surfaces, and (c) PSL in-plane. (d) High-resolution FE-TEM image of the PSL and an inset revealing its selected area diffraction pattern. (e) Raman spectrum and (f) XRD pattern of the PSL. XPS (g) C 1s, (h) O 1s, and (i) N 1s spectra of the PSL.

This result suggests the significant potential of the Na metal anode because not only does the system require no active material, electrolyte additive, conducting agent, or binder, but its electrochemical performance is also at a practical level. However, the Cu-foil-based electrode system requires a careful review and further development to optimize the cell-to-cell variation and cycling stability. For example, the effects of surface properties and nucleation sites on the Cu foil are unclear. Additionally, it remains unclear whether the introduction of catalytic sites can further increase the electrochemical performance. Zhang et al. reported that extrinsic defects in graphene-based materials can be nucleophilic sites for metal nucleation, leading to uniform metal development on the whole surface of the catalytic electrode materials.[30] In addition, Cohn et al. showed that a carbon layer on the Al substrate contributes to highly efficient and stable plating and stripping of Na metal, with its nucleation overpotential being reduced to ~12 mV compared with that (~19 mV) of the bare Al substrate.[31] These references indicate that carbon-based materials including defective carbon structures can result in the coincident growth of metal on their large surface areas, obstructing dendritic metal growth in a particular region with an uneven SEI layer or a large Na ion flux. Hence, it is expected that the combination of a glyme-based electrolyte and carbon-based catalytic materials could yield a notable result with high CEs and stable cycle lives. In our previous study, catalytic carbon nanomaterials with a macroporous structure, called as MC-CNTs, were introduced as a template guiding a stable metal plating/stripping process in a glyme-based electrolyte and showed a stable cycling performance over 1000 cycles with average CEs of 99.9%.[32] The electrochemical performance of the MC-CNTs was further demonstrated through a full-cell experiment using a polyanion cathode material, proving that their performance was at a practical level. However, for the practical application of metal anodes, more reliable cell performance with a low cell-to-cell variation and a simple method based on well-established technology are required. Moreover, the CEs need to be improved further. This can be achieved through the introduction of more catalytic active sites and ensuring a highly even and homogeneous interfacial area, as well as the introduction of nucleophilic active sites for better wettability of the glyme-based electrolyte.

In this study, a thin pyroprotein seed layer (PSL, ~100 nm thick) was coated on a Cu substrate via spin-coating with a regenerated silk fibroin (RSF) followed by pyrolysis at 800 °C. The PSLs were composed of highly disordered carbon building blocks in which Na ions can diffuse and come into contact with numerous defective carbon sites. Therefore, the homogeneous deposition of Na metal can be induced on the PSL-coated Cu electrode (PSL-Cu) at a high areal current density of ~4 mA cm^{-2}. The nucleation overpotential of PSL-Cu remarkably decreases by ~10 mV, which is a much lower value than that (~26 mV) of a bare Cu foil electrode. In addition, the PSL-Cu achieved stable Na metal deposition/dissolution during ~300 cycles with a mean CE of ~99.96%, which is the highest value reported for metal anodes thus far. Moreover, the PSL-based Na metal anode has a significantly low cell-to-cell variation with a CE deviation of ~0.43%. Considering the simple fabrication process and well-established chemistry of PSL-Cu, the electrochemical performance of PSL-Cu deserves significant attention. The feasibility of PSL-Cu was further demonstrated via a full-cell experiment using a reported polyanion cathode, which revealed a high specific energy of 402 W h kg^{-1} at 390 W kg^{-1}, high specific power of 3800 W kg^{-1} at 275 W h kg^{-1}, and stable cycling with a capacity retention of 86% after 30 cycles. This work proves that the electrochemical performance of a metal anode can be advanced by (1) increasing the number of catalytic nucleation sites for metal electrodeposition and (2) enhancing the wettability of the electrolyte through the introduction of a large number of nucleophilic functional groups.[33−35]

■ EXPERIMENTAL SECTION

Preparation of PSL-Cu. Cocoons of *Bombyx mori* silkworm silk were prepared by the reported method.[6] The final concentration of the silk fibroin aqueous solution was controlled to be 4.0 wt %. The RSF solution was thereafter spin-coated onto Cu foils at 4000 rpm. To control the thickness of the RSF thin film, 0.5, 1.0, and 2.0 wt % RSF solutions were also prepared and spin-coated onto Cu foils at 4000 rpm. The RSF-coated Cu foils were heated in a furnace at 800 °C under an inert gas flow (200 mL min^{-1}) by applying a heating rate of 5 °C min^{-1} and a holding time of 2 h at 800 °C. After the pyrolysis process of the RSF thin film, the resulting PSL-Cu was cooled down to ambient temperature under an inert gas flow and then kept in a vacuum oven at 30 °C.

Characterization. The RSF- and PSL-coated samples and their electrochemical performances were examined using several analytic
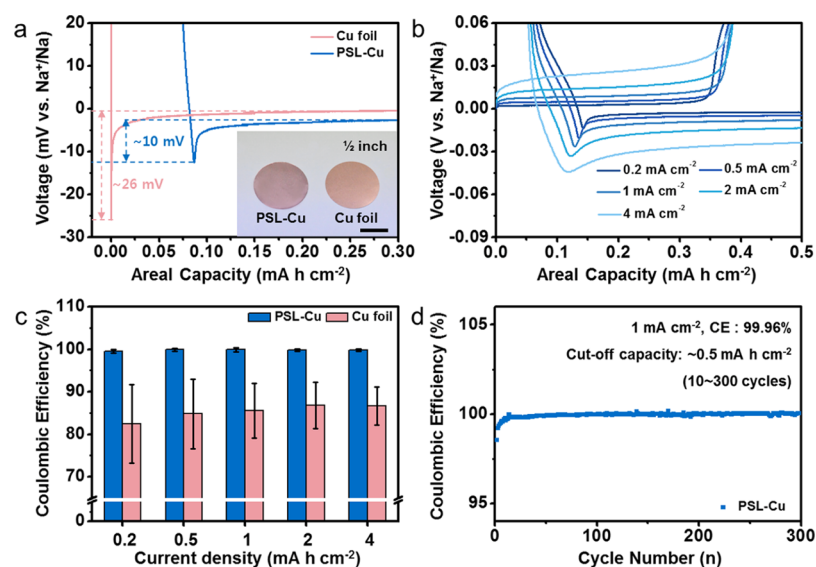
Figure 2. (a) Galvanostatic sodium metal plating profiles of Cu foil and PSL-Cu at a current rate of 50 μA cm^{-2}. (b) Rate performance of sodium metal deposition/stripping on PSL-Cu at current rates from 0.2 to 4 mA cm^{-2}. (c) CEs of Cu foil and PSL-Cu at current rates from 0.2 to 4 mA cm^{-2}. (d) Cycling stability of galvanostatic sodium metal plating/stripping cycles on PSL-Cu (a cutoff capacity of 0.5 mA h cm^{-2} was applied).

methods, which were described in the Supporting Information.[6,12,32,36]

RESULTS AND DISCUSSION

The silk fibroin thin film prepared from the 4 wt % RSF aqueous solution via spin-coating (4000 rpm) has a homogeneous thickness of ~500 nm as shown in Figure 1a. After pyrolysis at 800 °C, the chemical structure of the silk fibroin is drastically changed to a poly-aromatic hexagonal carbon-based structure and its thickness is significantly reduced by ~100 nm (Figure 1b).[37,38] Nevertheless, it is remarkable that the resulting PSL has a uniform thickness and highly even surface with a low root-mean-square roughness (R_{rms}) value of ~0.57 nm (Figure S1). The R_{rms} of the PSLs was affected by their thickness. When the thickness of the PSLs is lower than 100 nm, their R_{rms} values increase sharply (Figure S1). Therefore, the PSL was prepared with a thickness of ~100 nm for catalytic Na metal deposition/stripping. In-plane field emission scanning electron microscopy (FE-SEM) and optical images of the PSLs support their uniformity (Figures 1c and S2). The microstructure of the PSLs was confirmed using FE transmission electron microscopy (FE-TEM) images after being transferred onto a TEM grid, as shown in Figure 1d. A highly disordered carbon structure with no long-range graphitic ordering is confirmed using the FE-TEM image (Figure 1d), and the selected area diffraction pattern also supports the disordered structure of the PSLs (inset of Figure 1d). The detailed microstructure of the PSLs was further investigated using Raman spectra and X-ray diffraction (XRD) patterns. In the Raman spectrum (Figure 1e), distinct peak pairs were observed at 1359.6 and 1605.8 cm^{-1}, which correspond to the D and G bands, respectively. The D band originates from the disordered A_{1g} breathing mode of the poly-hexagonal carbon structures, whereas the G band originates from the E_{2g} vibration mode of the six-membered aromatic ring.[37] Therefore, the presence of D and G bands suggests that the hexagonal ring structures composed of sp^2-hybridized carbon atoms are well developed. Further, the D to G ratio (I_D/I_G) of the Raman spectrum provides information on the

lateral size (L_a) of the crystalline graphene domains.[38] The PSLs have an I_D/I_G value of 0.78, corresponding to an L_a of approximately 5.6 nm. In contrast to the Raman spectrum, which showed two distinct peaks, the XRD pattern of the PSLs showed a very broad graphite (002) peak around 22°, indicating hardly developed graphitic ordering of the carbon basic structural units (Figure 1f). The chemical structure of the PSLs was characterized using X-ray photoelectron spectroscopy (XPS) analysis (Figure 1g–i). In the C 1s spectrum, the main sp^2 C=C bonding was found at 284.4 eV, and sp^3 C–C, C–O/C–N, and O–C=O bonding were observed at 284.7, 285.9, and 289.6 eV, respectively (Figure 1g).[39] This result indicates that the PSLs have numerous heteroatoms and defective carbon structures. The O 1s spectrum confirms that the oxygen groups were composed of two groups based on C–O and C=O/O–C=O bonding (Figure 1h). In addition, the nitrogen groups exhibited two main configurations, pyridinic N and pyridonic N, and minor quaternary N and N-oxide structures (Figure 1i).[40] The C/O and C/N ratios were calculated to be 8.0 and 20.8, respectively. Considering the oxygen and nitrogen configurations, a model structure of the carbon basic structural unit that constitutes the PSLs is depicted in Figure S3. The highly functionalized carbon structures of the PSLs could induce highly efficient catalytic effects, which result in homogeneous metal growth over the entire electrode surface.

The electrochemical performances of the PSL-Cu and Cu foil electrodes as Na metal anodes were tested in an electrolyte of 1 M NaPF$_6$ dissolved in diethylene glycol dimethyl ether (DEGDME) without additives, with a cutoff capacity of 0.5 mA h cm^{-2}. A photograph of both electrodes shows no morphological difference (inset of Figure 2a), whereas their electrochemical performances are significantly different. The first Na metal plating profiles of both electrodes at an areal current density of 50 μA cm^{-2} exhibit voltage overshooting (VO) in their early parts, which originates from the nucleation barrier of electrochemically reduced Na metal (Figure 2a).[32] Therefore, a lower VO indicates a better catalytic effect. The PSL-Cu has a remarkably low VO and overpotential of ~10
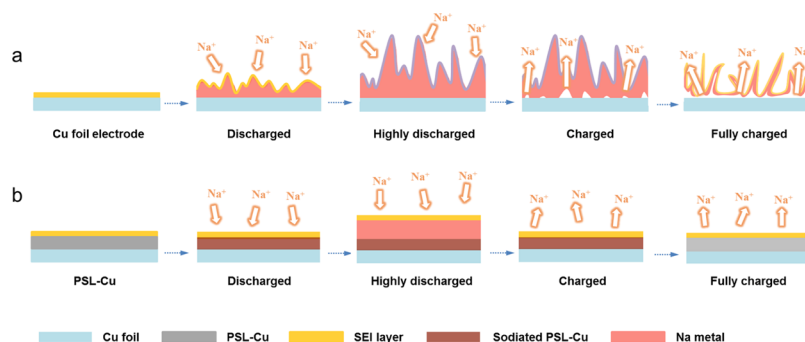
Figure 3. Schematic image for the sodium metal plating/stripping process on (a) Cu foil and (b) PSL-Cu electrodes.

mV, which is a much lower value than that (~26 mV) of the Cu foil electrode. This result suggests that sodium metal deposition on PSL-Cu is much more favorable than on Cu foil. The pyroprotein layer can play three important roles in the sodium metal deposition process. First, the heteroatom-enriched carbon structure has greater hydrophilicity, leading to a more similar surface energy between PSL-Cu and the electrolyte. As indicated by the following equation, $\frac{\Delta H_{mix}}{V_{mix}} \approx \frac{2}{T_G}(\delta_G - \delta_{sol})^2 \varnothing$, where $\delta_i = \sqrt{E_{sur}^i}$ is the square root of the surface energy of phase i, T_G and $\varnothing$ are the thickness and volume fraction of PSL-Cu, respectively, and ΔH_{mix} and V_{mix} are enthalpy and volume of mixing, respectively, and the similar surface energy indicates high compatibility between PSL-Cu and the electrolyte. Therefore, the PSL-Cu could have a good wettability in the glyme-based electrolyte, guiding the homogeneous sodium metal deposition. Second, it dramatically increases the active surface area because sodium ions can be inserted into the disordered carbon layers. Third, the defective structures of PSL-Cu act as highly effective catalytically active sites for metal deposition. Therefore, although the electrical conductivity (9.3×10^0 S cm^{-1}) of PSL-Cu is several orders of magnitude smaller than that of bare Cu foil, sodium metal is preferentially deposited on the PSL-Cu surface. However, the relatively low electrical conductivity induces greater polarization than the Cu foil electrode, leading to the higher voltage drop observed in the discharge profile of PSL-Cu. Nevertheless, the overpotential is not increased much with increasing current rates (Figure 2b). At a current rate 80 times higher (4 mA cm^{-2}), the PSL-Cu exhibited a nucleation overpotential of only 23 mV (Figure 2b). The drastic reduction of the VO could be caused by the presence of numerous active sites. The first-order linear equation exhibited in a previous report describes Na metal nucleation process.[41] From the equation, the Na metal growth mechanism can be differentiated into three different types according to the characteristic times of diffusion and charge transfer: (1) kinetic control ($k_G/DN_0^{1/2} \ll 1$), (2) mixed kinetic-diffusion control ($k_G/DN_0^{1/2} \approx 1$), and (3) diffusion control ($k_G/DN_0^{1/2} \gg 1$).[41,42] According to the literature, Na metal growth by the kinetic-controlled system can induce a filmlike metal deposition on the surface of the electrode.[41,42] In addition, the kinetic-controlled metal deposition can be induced by introduction of a lot of catalytic active sites. It is well-known that defective carbon structures can act as redox centers for Na ion storage in the anodic voltage region.[6−9] When the cell voltage decreases in the anodic voltage region close to 0 V versus Na$^+$/Na, numerous Na ions are chemisorbed on the surface of the defective carbon structures.[6] Furthermore, as the voltage

further decreases to ≤0 V, Na metal could be deposited on the carbon surface. At this time, the Na-introduced sites could act as catalytic sites for the deposition of Na metal. In the first Na metal deposition profile of the PSL-Cu, the areal capacity is 0.087 mA h cm^{-2}, corresponding to 3.25×10^{-6} mol cm^{-2} of Na ions (approximately 1.95×10^{18} ea). If the sodiated sites fully work as catalytic spots, dendrite-free metal growth is possible because the numerous catalytic sites enable a homogenous Na ion flux and simultaneous metal growth in the over the entire electrode area. From a macroscopic viewpoint, filmlike metal layers could be formed/stripped in the electrochemical cycling process. The filmlike metal deposition morphology was directly confirmed by ex situ characterization. To obtain an ex situ FE-SEM image of the fracture surface after sodium metal deposition on PSL-Cu, sodium metal was deposited on PSL-Cu with an areal capacity of 0.5 mA h cm^{-2} in a 2032-type coin cell and then disassembled in Ar atmosphere. The PSL-Cu with sodium metal was mounted on a SEM holder, coated with DEGDME electrolyte to obstruct its exposure to air, and then transferred to the SEM instrument. As shown in Figure S4, the ex situ SEM image reveals a clear sodium metal layer on the surface of PSL-Cu. The energy-dispersive spectrometer images also indicate that sodium and carbon are mainly located in separate layers. In addition, an optical microscopy image of PSL-Cu after sodium electrodeposition with an areal capacity of 0.5 mA h cm^{-2} shows a filmlike metal layer (Figure S5). In contrast, under the same conditions, dendritic metals were formed on the surface of bare Cu foil. Ex situ FE-SEM images also demonstrate the catalytic effects of PSL-Cu (Figure S6). After 100 cycles of sodium metal deposition/stripping, the PSL-Cu retained its initial morphology, while the bare Cu foil was contaminated with moss-like byproducts. These results demonstrate that the pyroprotein layers play an important role in the Na metal plating/dissolution cycles. However, a similar experiment using a carbonate-based electrolyte led to poor CE values (Figure S7). Hence, the high electrochemical performance of PSL-Cu is induced by a synergistic effect with the glyme-based electrolyte.

On the basis of both the theoretical background and experimental results, the concepts of specific sodium metal deposition/stripping on both PSL-Cu and Cu foil electrodes are depicted as a schematic image in Figure 3. The Cu foil electrode is poor in catalytic sites for the nucleation of Na metal, which could result in a heterogeneous metal growth with protruding sections during the metal deposition process. As the Na ion flux tends to converge on projecting areas, the uneven metallic surface of the Cu foil electrode could

accelerate dendritic metal growth in the continuous metal deposition process (Figure 3a).[25]

The reversibility of Na metal stripping from the high aspect ratio dendritic metals is so poor that a drastic decrease in the CE could occur with the accumulation of mossy byproducts (Figure 3a). In contrast, the PSL-Cu with its numerous catalytic sites can result in homogeneous metal growth over the entire surface area, causing highly reversible metal plating/stripping cycles (Figure 3b). The CEs and cell-to-cell variations of the PSL-Cu and Cu foil electrodes were characterized at different current rates from 0.2 to 4 mA cm^{-2} using 10 cells for the respective samples, as shown in Figure 2c. At current rates of 0.5 and 1 mA cm^{-2}, the PSL-Cu electrode shows high average CEs of 99.9%, whereas the Cu foil electrode exhibits CEs of approximately 85% at the same current rates. The CEs of the Cu foil are much lower than those previously reported.[26] Higher CEs could probably be induced by pretreatment and/or surface modification of the Cu foil. The type of Cu foil and its surface uniformity probably affect the electrochemical performance. However, there is no information regarding such treatments in the report, which makes comparison difficult. Hence, we reiterate that the commercial Cu foil electrode (Wellcos Corp. Seoul, Korea) in this study was used without further treatment.

It is noteworthy that the PSL-Cu electrode shows similar CEs with a standard deviation of ∼0.43% in repeated cell tests, whereas the Cu foil electrodes show at least 10 times greater cell-to-cell variations in their CEs (Figure 2c). Although several issues arise with regard to the decrease in the CE, one major origin of the large CE deviation could be due to the dendritic metal growth. In a Cu foil electrode with low catalytic sites, the diffusion-controlled Na metal deposition is accompanied by the growth of dendritic structures. In addition, the uneven surface could induce an inhomogeneous Na ion flux, which leads to the dendritic Na metal growth. The reproducibility of the electrochemical performance is a critical factor for the practical application of metal anodes. The PSL-Cu electrode shows not only high CEs at a viable current rate but also reliable cell performance in repeated tests. The cycling performance of the PSL-Cu electrode for continuous Na metal deposition/stripping was examined at a current rate of 1 mA cm^{-2} during 300 cycles (Figure 2d). After achieving stability in the early few cycles, the average CE of the PSL-Cu electrode reached ∼99.96%, and stable cycling was maintained throughout the entire cycling process. The voltage profile versus time plot, shown in Figure S8, supports the PSL-Cu cycling stability analysis. In addition, stable cycling was maintained with an increased cutoff capacity of 1 mA h cm^{-2}, while a slight fluctuation of the CE was observed at 2 mA h cm^{-2} (Figure S9).

The practicality of PSL-Cu was further tested using a full cell assembled with a reported cathode material, Na$_{1.5}$VPO$_{4.8}$F$_{0.7}$.[43] As shown in Figure 4a, the galvanostatic charge/discharge profiles of the Na$_{1.5}$VPO$_{4.8}$F$_{0.7}$ cathode at a specific current rate of 0.1 A g^{-1} over a voltage range of 2.5−4.4 V versus Na$^+$/Na show a specific capacity of ∼105 mA h g^{-1} and an average voltage of ∼3.9 V in a half-cell test with a Na metal foil as the reference and counter electrodes. A full cell was prepared using PSL-Cu and Na$_{1.5}$VPO$_{4.8}$F$_{0.7}$ as the anode and cathode, respectively, after precycling of the respective electrodes for 10 cycles, and an electrolyte of 1 M NaPF$_6$ dissolved in DEGDME was used for the test. The PSL-Cu//Na$_{1.5}$VPO$_{4.8}$F$_{0.7}$ cell shows similar galvanostatic charge/
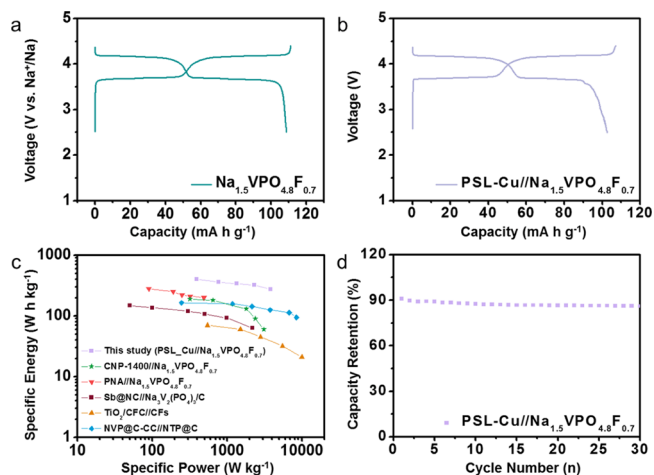
Figure 4. Galvanostatic charge/discharge profiles of (a) Na$_{1.5}$VPO$_{4.8}$F$_{0.7}$ and (b) PSL-Cu//Na$_{1.5}$VPO$_{4.8}$F$_{0.7}$ cells over a voltage window of 2.5−4.4 V at a current rate of 0.1 A g^{-1}. (c) Ragone plots of several energy storage devices including the PSL-Cu//Na$_{1.5}$VPO$_{4.8}$F$_{0.7}$ cell. (d) Cycling performance of the PSL-Cu//Na$_{1.5}$VPO$_{4.8}$F$_{0.7}$ cell at a current rate of 0.2 A g^{-1}.

discharge profiles to the Na$_{1.5}$VPO$_{4.8}$F$_{0.7}$ cathode (Figure 4b), wherein a specific capacity of ∼103 mA h g^{-1} and an average voltage of ∼3.9 V were achieved at a current rate of 0.1 A g^{-1} over the voltage window 2.5−4.4 V (Figure 4b). This corresponds to a specific energy of 402 W h kg^{-1} at 390 W kg^{-1} for active material-based calculations. The remarkably high specific energy is partly due to the negligible loading content of the thin catalytic seed layer coated on the substrate, which can maximize the specific energy of the full cell. Furthermore, the specific power of the PSL-Cu//Na$_{1.5}$VPO$_{4.8}$F$_{0.7}$ cell reached 3800 W kg^{-1} at 275 W h kg^{-1}, which is a much higher value compared with the previously reported results obtained for CNP-1400//Na$_{1.5}$VPO$_{4.8}$F$_{0.7}$,[6] PNA//Na$_{1.5}$VPO$_{4.8}$F$_{0.7}$,[12] Sb@NC//Na$_3$V$_2$(PO$_4$)$_3$/C,[44] TiO$_2$/CFC//CFs,[45] and NVP@C-CC//NTP@C.[46] The energy−power relationship can be confirmed using the Ragone plot shown in Figure 4c. The cycling performance of the PSL-Cu//Na$_{1.5}$VPO$_{4.8}$F$_{0.7}$ cell was tested with a cutoff voltage of >4.4 and <2.5 V in the charge and discharge processes, respectively (Figure 4d). To clarify the cycling behavior of the full cell, the cycling performance of the Na$_{1.5}$VPO$_{4.8}$F$_{0.7}$ cathode was also determined at the same cutoff voltage, but at different current rates of 0.2, 0.5, and 1 A g^{-1} (Figure S10). The cathode showed no reduction in capacity over 100 cycles. Moreover, in the case of the full cell, limited Na ions originating from the Na$_{1.5}$VPO$_{4.8}$F$_{0.7}$ cathode are reversibly deposited/stripped on the PSL-Cu. Therefore, the loss of Na ions is directly connected to the reduction in capacity owing to the finite Na supply. The PSL-Cu//Na$_{1.5}$VPO$_{4.8}$F$_{0.7}$ cell maintains approximately 86% of the initial capacity after 30 cycles, corresponding to a CE of 99.5% (calculated from $(0.995)^{30}$). Hence, the thin PSL on the Cu substrate drastically improves the reversibility of the Na ion deposition/stripping cycles.

■ CONCLUSIONS

In summary, a thin RSF coated onto a Cu foil was transformed into a homogeneous pyroprotein layer with a thickness of ∼100 nm and an R_{rms} value of ∼0.57 nm. The PSL-Cu electrode was highly stable during Na metal deposition/

stripping cycles in an electrolyte of 1 M $NaPF_6$ dissolved in DEGDME, with a low nucleation overpotential of ~10 mV and average CEs of ~99.96% over 300 cycles, except for during a few initial cycles, could be achieved. In addition, the PSL-Cu electrode showed remarkably low cell-to-cell CE variations of ~0.43%, demonstrating the necessity of the catalytic PSLs. Moreover, the full-cell tests based on PSL-Cu// $Na_{1.5}VPO_{4.8}F_{0.7}$ showed a specific energy of 402 W h kg^{-1} at 390 W kg^{-1} and a specific power of 3,800 W kg^{-1} at 275 W h kg^{-1}, with a capacity retention of 86% after 30 cycles.

■ ASSOCIATED CONTENT

ⓢ Supporting Information

The Supporting Information is available free of charge on the ACS Publications website at DOI: 10.1021/acsami.8b15938.

Additional information such as characterization method, surface topography data, optical images, schematic image, ex situ FE-SEM images, and electrochemical results of PSL-Cu (PDF)

■ AUTHOR INFORMATION

Corresponding Authors
*E-mail: hjjin@inha.ac.kr (H.-J.J.).
*E-mail: ysyun@kangwon.ac.kr (Y.S.Y.).

ORCID ⓘ
Min Eui Lee: 0000-0002-1696-1397
Hyo Won Kwak: 0000-0002-6423-0687
Jin Hwan Kwak: 0000-0002-7934-1523
Hyoung-Joon Jin: 0000-0002-1763-9455
Young Soo Yun: 0000-0002-2937-9638

Present Address
⊥Department of Forest Sciences, Seoul National University, Seoul 08826, South Korea

Author Contributions
§M.E.L. and H.W.K. contributed equally to this work.

Notes
The authors declare no competing financial interest.

■ ACKNOWLEDGMENTS

■ REFERENCES

(1) Yabuuchi, N.; Kubota, K.; Dahbi, M.; Komaba, S. Research Development on Sodium-Ion Batteries. *Chem. Rev.* **2014**, *114*, 11636−11682.

(2) Kubota, K.; Komaba, S. Review-Practical Issues and Future Perspective for Na-Ion Batteries. *J. Electrochem. Soc.* **2015**, *162*, A2538−A2550.

(3) Kim, S.-W.; Seo, D.-H.; Ma, X.; Ceder, G.; Kang, K. Electrode Materials for Rechargeable Sodium-Ion Batteries: Potential Alternatives to Current Lithium-Ion Batteries. *Adv. Energy Mater.* **2012**, *2*, 710−721.

(4) Komaba, S.; Murata, W.; Ishikawa, T.; Yabuuchi, N.; Ozeki, T.; Nakayama, T.; Ogata, A.; Gotoh, K.; Fujiwara, K. Electrochemical Na Insertion and Solid Electrolyte Interphase for Hard-Carbon Electrodes and Application to Na-Ion Batteries. *Adv. Funct. Mater.* **2011**, *21*, 3859−3867.

(5) Xia, X.; Dahn, J. R. A Study of the Reactivity of De-Intercalated $NaNi_{0.5}Mn_{0.5}O_2$ with Non-Aqueous Solvent and Electrolyte by Accelerating Rate Calorimetry. *J. Electrochem. Soc.* **2012**, *159*, A1048−A1051.

(6) Yun, Y. S.; Park, K.-Y.; Lee, B.; Cho, S. Y.; Park, Y.-U.; Hong, S. J.; Kim, B. H.; Gwon, H.; Kim, H.; Lee, S.; Park, Y. W.; Jin, H.-J.; Kang, K. Sodium-Ion Storage in Pyroprotein-Based Carbon Nanoplates. *Adv. Mater.* **2015**, *27*, 6914−6921.

(7) Yun, Y. S.; Park, Y.-U.; Chang, S.-J.; Kim, B. H.; Choi, J.; Wang, J.; Zhang, D.; Braun, P. V.; Jin, H.-J.; Kang, K. Crumpled Graphene Paper for High Power Sodium Battery Anode. *Carbon* **2016**, *99*, 658−664.

(8) Wen, Y.; He, K.; Zhu, Y.; Han, F.; Xu, Y.; Matsuda, I.; Ishii, Y.; Cumings, J.; Wang, C. Expanded Graphite as Superior Anode for Sodium-Ion Batteries. *Nat. Commun.* **2014**, *5*, 4033.

(9) Lotfbad, E. M.; Ding, J.; Cui, K.; Kohandehghan, A.; Kalisvaart, W. P.; Hazelton, M.; Mitlin, D. High-Density Sodium and Lithium Ion Battery Anodes from Banana Peels. *ACS Nano* **2014**, *8*, 7115−7129.

(10) Wang, Y.; Yu, X.; Xu, S.; Bai, J.; Xiao, R.; Hu, Y.-S.; Li, H.; Yang, X.-Q.; Chen, L.; Huang, X. A Zero-Strain Layered Metal Oxide as the Negative Electrode for Long-Life Sodium-Ion Batteries. *Nat. Commun.* **2013**, *4*, 2365.

(11) Jiang, Y.; Hu, M.; Zhang, D.; Yuan, T.; Sun, W.; Xu, B.; Yan, M. Transition Metal Oxides for High Performance Sodium Ion Battery Anodes. *Nano Energy* **2014**, *5*, 60−66.

(12) Choi, J.; Kim, N. R.; Lim, K.; Ku, K.; Yoon, H. J.; Kang, J. G.; Kang, K.; Braun, P. V.; Jin, H.-J.; Yun, Y. S. Tin Sulfide-Based Nanohybrid for High-Performance Anode of Sodium-Ion Batteries. *Small* **2017**, *13*, 1700767.

(13) Kim, N. R.; Choi, J.; Yoon, H. J.; Lee, M. E.; Son, S. U.; Jin, H.-J.; Yun, Y. S. Conversion Reaction of Copper Sulfide Based Nanohybrids for Sodium-Ion Batteries. *ACS Sustainable Chem. Eng.* **2017**, *5*, 9802−9808.

(14) Yu, D. Y. W.; Prikhodchenko, P. V.; Mason, C. W.; Batabyal, S. K.; Gun, J.; Sladkevich, S.; Medvedev, A. G.; Lev, O. High-Capacity Antimony Sulphide Nanoparticle-Decorated Graphene Composite as Anode for Sodium-Ion Batteries. *Nat. Commun.* **2013**, *4*, 2922.

(15) Kim, Y.; Kim, Y.; Choi, A.; Woo, S.; Mok, D.; Choi, N.-S.; Jung, Y. S.; Ryu, J. H.; Oh, S. M.; Lee, K. T. Tin Phosphide as a Promising Anode Material for Na-Ion Batteries. *Adv. Mater.* **2014**, *26*, 4139−4144.

(16) Li, W.; Chou, S.-L.; Wang, J.-Z.; Kim, J. H.; Liu, H.-K.; Dou, S.-X. $Sn_{4+x}P_3$ @ Amorphous Sn-P Composites as Anodes for Sodium-Ion Batteries with Low Cost, High Capacity, Long Life, and Superior Rate Capability. *Adv. Mater.* **2014**, *26*, 4037−4042.

(17) Farbod, B.; Cui, K.; Kalisvaart, W. P.; Kupsta, M.; Zahiri, B.; Kohandehghan, A.; Lotfabad, E. M.; Li, Z.; Luber, E. J.; Mitlin, D. Anodes for Sodium Ion Batteries Based on Tin-Germanium-Antimony Alloys. *ACS Nano* **2014**, *8*, 4415−4429.

(18) Liu, Y.; Zhang, N.; Jiao, L.; Tao, Z.; Chen, J. Ultrasmall Sn Nanoparticles Embedded in Carbon as High-Performance Anode for Sodium-Ion Batteries. *Adv. Funct. Mater.* **2014**, *25*, 214−220.

(19) Abel, P. R.; Lin, Y.-M.; de Souza, T.; Chou, C.-Y.; Gupta, A.; Goodenough, J. B.; Hwang, G. S.; Heller, A.; Mullins, C. B. Nanocolumnar Germanium Tin Films as a High-Rate Sodium-Ion Battery Anode Material. *J. Phys. Chem. C* **2013**, *117*, 18885−18890.

(20) Qian, J.; Wu, X.; Cao, Y.; Ai, X.; Yang, H. High Capacity and Rate Capability of Amorphous Phosphorus for Sodium Ion Batteries. *Angew. Chem., Int. Ed.* **2013**, *125*, 4731−4734.

(21) Sun, J.; Lee, H.-W.; Pasta, M.; Yuan, H.; Zheng, G.; Sun, Y.; Li, Y.; Cui, Y. A Phosphorene-Graphene Hybrid Material as a High-Capacity Anode for Sodium-Ion Batteries. *Nat. Nanotechnol.* **2015**, *10*, 980−985.

(22) Park, Y.; Shin, D.-S.; Woo, S. H.; Choi, N. S.; Shin, K. H.; Oh, S. M.; Lee, K. T.; Hong, S. Y. Sodium Terephthalate as an Organic Anode Material for Sodium Ion Batteries. *Adv. Mater.* **2012**, *24*, 3562−3567.

(23) He, K.; Zhou, Y.; Gao, P.; Wang, L.; Pereira, N.; Amatucci, G. G.; Nam, K.-W.; Yang, X.-Q.; Zhu, Y.; Wang, F.; Su, D. Sodiation via

Heterogeneous Disproportionation in FeF_2 Electrodes for Sodium-Ion Batteries. *ACS Nano* **2014**, *8*, 7251−7259.

(24) Zhu, Z.; Li, H.; Liang, J.; Tao, Z.; Chen, J. The Disodium Salt of 2,5-dihydroxy-1,4-benzoquinone as Anode Material for Rechargeable Sodium Ion Batteries. *Chem. Commun.* **2015**, *51*, 1446−1448.

(25) Zhang, J.-G.; Xu, W.; Henderson, W. A. *Lithium Metal Anodes and Rechargeable Lithium Metal Batteries*; Springer: Switzerland, 2017.

(26) Seh, Z. W.; Sun, J.; Sun, Y.; Cui, Y. A Highly Reversible Room-Temperature Sodium Metal Anode. *ACS Cent. Sci.* **2015**, *1*, 449−455.

(27) Luo, W.; Lin, C.-F.; Zhao, O.; Noked, M.; Zhang, Y.; Rubloff, G. W.; Hu, L. Ultrathin Surface Coating Enables the Stable Sodium Metal Anode. *Adv. Energy Mater.* **2016**, *7*, 1601526.

(28) Cao, R.; Mishra, K.; Li, X.; Qian, J.; Engelhard, M. H.; Bowden, M. E.; Han, K. S.; Mueller, K. T.; Henderson, W. A. Enabling Room Temperature Sodium Metal Batteries. *Nano Energy* **2016**, *30*, 825−830.

(29) Chi, S.-S.; Liu, Y.; Song, W.-L.; Fan, L.-Z.; Zhang, Q. Prestoring Lithium into Stable 3D Nickel Foam Host as Dendrite-Free Lithium Metal Anode. *Adv. Funct. Mater.* **2017**, *27*, 1700348.

(30) Zhang, R.; Chen, X.-R.; Chen, X.; Cheng, X.-B.; Zhang, X.-Q.; Yan, C.; Zhang, Q. Lithiophilic Sites in Doped Graphene Guide Uniform Lithium Nucleation for Dendrite-Free Lithium Metal Anodes. *Angew. Chem., Int. Ed.* **2017**, *56*, 7764−7768.

(31) Cohn, A. P.; Muralidharan, N.; Carter, R.; Share, K.; Pint, C. L. Anode-Free Sodium Battery through in Situ Plating of Sodium Metal. *Nano Lett.* **2017**, *17*, 1296−1301.

(32) Yoon, H. J.; Kim, N. R.; Jin, H.-J.; Yun, Y. S. Macroporous Catalytic Carbon Nanotemplates for Sodium Metal Anodes. *Adv. Energy Mater.* **2017**, *8*, 1701261.

(33) Wang, T.; Salvatierra, R. V.; Jalilov, A. S.; Tian, J.; Tour, J. M. Ultrafast Charging High Capacity Asphalt-Lithium Metal Batteries. *ACS Nano* **2017**, *11*, 10761−10767.

(34) Dong, Q.; Hong, B.; Fan, H.; Gao, C.; Hong, S.; Lai, Y. Electron-Rich Functional Doping Carbon Host as Dendrite-Free Lithium Metal Anode. *Electrochim. Acta* **2018**, *284*, 376−381.

(35) Zheng, Z.; Zeng, X.; Ye, H.; Cao, F.; Wang, Z. Nitrogen and Oxygen Co-doped Graphitized Carbon Fibers with Sodiophilic-Rich Sites Guide Uniform Sodium Nucleation for Ultrahigh-Capacity Sodium-Metal Anodes. *ACS Appl. Mater. Interfaces* **2018**, *10*, 30417−30425.

(36) Choe, J. H.; Kim, N. R.; Lee, M. E.; Yoon, H. J.; Song, M. Y.; Jin, H.-J.; Yun, Y. S. Flexible Graphene Stacks for Sodium-Ion Storage. *ChemElectroChem* **2017**, *4*, 716−720.

(37) Cho, S. Y.; Yun, Y. S.; Lee, S.; Jang, D.; Park, K.-Y.; Kim, J. K.; Kim, B. H.; Kang, K.; Kaplan, D. L.; Jin, H.-J. Carbonization of a Stable β-sheet-rich Silk Protein into a Pseudographitic Pyroprotein. *Nat. Commun.* **2015**, *6*, 7145.

(38) Cho, S. Y.; Yun, Y. S.; Jang, D.; Jeon, J. W.; Kim, B. H.; Lee, S.; Jin, H.-J. Ultra Strong Pyroprotein Fibres with Long-Range Ordering. *Nat. Commun.* **2017**, *8*, 74.

(39) Kim, N. R.; Lee, S. M.; Kim, M. W.; Yoon, H. J.; Hong, W. G.; Kim, H. J.; Choi, H. J.; Jin, H.-J.; Yun, Y. S. Amphicharge-Storable Pyropolymers Containing Multitered Nanopores. *Adv. Energy Mater.* **2017**, *7*, 1700629.

(40) Lee, M. E.; Jin, H.-J.; Yun, Y. S. Synergistic Catalytic Effects of Oxygen and Nitrogen Functional Groups on Active Carbon Electrodes for All-Vanadium Redox Flow Batteries. *RSC Adv.* **2017**, *7*, 43227−43232.

(41) Yoon, H. J.; Hong, S. K.; Lee, M. E.; Hwang, J.; Jin, H.-J.; Yun, Y. S. Sulfur-Doped Carbon Nanotemplates for Sodium Metal Anodes. *ACS Appl. Energy Mater.* **2018**, *1*, 1846−1852.

(42) Altimari, P.; Pagnanelli, F. Electrochemical Nucleation and Three-Dimensional Growth of Metal Nanoparticles under Mixed Kinetic-Diffusion Control: Model Development and Validation. *Electrochim. Acta* **2016**, *206*, 116−126.

(43) Park, Y.-U.; Seo, D.-H.; Kwon, H.-S.; Kim, B.; Kim, J.; Kim, H.; Kim, I.; Yoo, H.-I.; Kang, K. New High-Energy Cathode for a Na-Ion Battery with Ultrahigh Stability. *J. Am. Chem. Soc.* **2013**, *135*, 13870−13878.

(44) Xu, X.; Dou, Z.; Gu, E.; Si, L.; Zhou, X.; Bao, J. Uniformly-Distributed Sb Nanoparticles in Ionic Liquid-Derived Nitrogen-Enriched Carbon for Highly Reversible Sodium Storage. *J. Mater. Chem. A* **2017**, *5*, 13411−13420.

(45) Liu, S.; Luo, Z.; Tian, G.; Zhu, M.; Cai, Z.; Pan, A.; Liang, S. TiO_2 Nanorods Grown on Carbon Fiber Cloth as Binder-Free Electrode for Sodium-Ion Batteries and Flexible Sodium-Ion Capacitors. *J. Power Sources* **2017**, *363*, 284−290.

(46) Guo, D.; Qin, J.; Yin, Z.; Bai, J.; Sun, Y.-K.; Cao, M. Achieving High Mass Loading of $Na_3V_2(PO_4)_3$@Carbon on Carbon Cloth by Constructing Three-Dimensional Network between Carbon Fibers for Ultralong Cycle-Life and Ultrahigh Rate Sodium-Ion Batteries. *Nano Energy* **2018**, *45*, 136−147.